IOP Publishing Bioinspir. Biomim. 15 (2020) 065001 https://doi.org/10.1088/1748-3190/aba8ab

Bioinspiration & Biomimetics

CrossMark

RECEIVED
17 April 2020

REVISED
23 June 2020

ACCEPTED FOR PUBLICATION
23 July 2020

PUBLISHED
11 September 2020

PAPER

Rapid two-anchor crawling from a milliscale prismatic-push–pull (3P) robot

Wei Zhou and Nick Gravish[1]

Department of Mechanical & Aerospace Engineering, University of California at San Diego, CA, 92093 United States of America

[1] Author to whom any correspondence should be addressed.

E-mail: ngravish@ucsd.edu

Keywords: crawling, milliscale robots, anisotropic friction

Abstract

Many crawling organisms such as caterpillars and worms use a method of movement in which two or more anchor points alternately push and pull the body forward at a constant frequency. In this paper we present a milliscale push–pull robot which is capable of operating across a wide range of actuation frequencies thus enabling us to expand our understanding of two-anchor locomotion beyond the low-speed regime. We designed and fabricated a milliscale robot which uses anisotropic friction at two oscillating contact points to propel itself forward in a push–pull fashion. In experiments we varied the oscillation frequency, f, over a wide range (10–250 Hz) and observe a non-linear relationship between robot speed over this full frequency range. At low frequency ($f < 100$ Hz) forward speed increased linearly with frequency. However, at an intermediate push–pull frequency ($f > 100$ Hz) speed was relatively constant with increasing frequency. Lastly, at higher frequency ($f > 170$ Hz) the linear speed–frequency relationship returned. The speed–frequency relationship at low actuation frequencies is consistent with previously described two-anchor models and experiments in biology and robotics, however the higher frequency behavior is inconsistent with two-anchor frictional behavior. To understand the locomotion behavior of our system we first develop a deterministic two-anchor model in which contact forces are determined exactly from static or dynamic friction. Our experiments deviate from the model predictions, and through 3D kinematics measurements we confirm that ground contact is intermittent in robot locomotion at higher frequencies. By including probabilistic foot slipping behavior in the two-anchor friction model we are able to describe the three-regimes of robot locomotion.

1. Introduction

Terrestrial organisms use a multitude of locomotion strategies to move such as walking and running on legs, lateral undulations of the body while slithering, and longitudinal body oscillations during crawling [1]. Ground-based bioinspired robots employ many of the same principles—legs, lateral undulations, and longitudinal undulations. The actuation and control of bioinspired robots in many cases have been informed, and even improved by observations of their biological counterparts. For example the spring-mass dynamics of legged locomotion have informed robot mechanism and control design [2, 3], the flapping and fixed wing aerodynamics of flight have improved aerial robots [4–6], and slithering strategies of snakes have enabled snake-like robots to traverse challenging terrain [7, 8]. However, when robots possess actuation, sensory, or control capabilities that supersede the capabilities of the biological system movement behaviors can be pushed to regimes not observed in nature [9]. Robots that are capable of extremal locomotion behavior, pushing far beyond the observed regimes of their biological counterparts, can enable us to test the generality of locomotion models across a wide range.

Crawling locomotion is broadly defined as movement across a surface in which forward progression is enabled by body movements rather than limb movements [1]. A diverse array of animals demonstrate crawling locomotion including insect larvae [10], worms [11], clams [12, 13], and snakes [14]. Similarly, many bioinspired crawling robots have been built and studied across a wide array of mechanical designs including soft-bodied, origami, and rigid crawling robots [15–19]. Crawling locomotion is

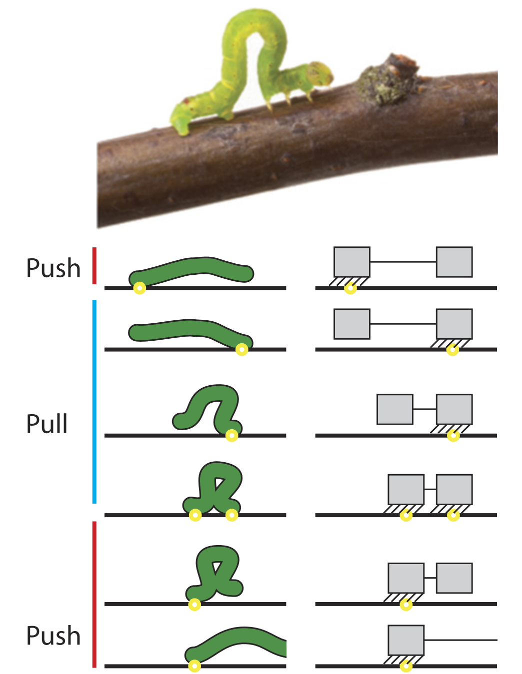

Figure 1. An inchworm uses a push–pull strategy of movement (top). Alternating contact points allow the body to be pushed or pulled forward (bottom left). A simple representation of inchworm crawling is a linear motion of two contact elements that alternate contact with the ground through anisotropic friction (bottom right). (Top image reproduced with permission from depositphotos. (c) Fotofermer (Vadim Dreznol)')

typically slow compared to legged locomotion because crawling requires reconfiguration and movement of large body segments (figure 1).

A common model used to describe the crawling dynamics of animals and robots is that of a two-anchor system in which two contact points successively push, and then pull the body forward in a repeating pattern (figure 1) [20–23]. The two points can independently anchor to the ground to support both body-weight and the required friction force for push–pull advancement. Successful crawling requires some forms of symmetry breaking within the push–pull cycle so that thrust forces can exceed frictional resistance. For example, many animals and robots will lift the body during the push or pull phase thus reducing body friction during advancement [24–26]. Theoretical models of two-anchor locomotion have explored symmetry breaking methods such as time asymmetry (rapid extension, slow contraction) [21], and alternating the magnitude of push and pull friction forces through mass-swapping [23], or directional and velocity dependent forces [27].

Anisotropic frictional contacts with the ground is another method employed by animals and robots so that symmetric push and pull sliding movements can generate forward motion through asymmetric friction [28–32]. Anisotropic friction is one of the keys to snake locomotion during longitudinal gaits [33]. A simple mechanism to generate frictional anisotropy is through angled contact points with the ground, such as has been used in the class of vibration based robots known as bristle-bots [34, 35]. Moreover, vibration based robots can also take advantage of dynamic resonance properties of their actuators, and when coupled with anisotropic friction this can further enhance locomotion capabilities [36, 37]. Thus, forward propulsion in two-anchor robot and animal systems can emerge from contact mechanics, body actuation dynamics, or combinations of both.

Many forms of bio-inspired crawling robots have been developed. The most prevalent bio-inspired crawling robots are inspired from soft-bodied crawling animals such as worms and larvae. These soft-bodied robots are often constructed from soft elastomers that are cast or 3D printed [24, 38–41], and they are actuated through pneumatic [38, 41–43], smart actuators such as shape memory alloys [26, 44–46], or dielectric elastomers [47, 48]. While soft bodies enable a wide range of body flexibility for crawling locomotion [49], actuation speed is a fundamental challenge in soft robotics [50]. Thus, many of the bio-inspired crawling robots move relatively slowly. Recent developments in small, lightweight, laminate robot fabrication [51] coupled with high-bandwidth piezoelectric (PZT) actuation [52] have enabled new ground-based mobile robots capable of extremely high speeds relative to their body size [9, 53]. The design and incorporation of flexure hinges that emulate revolute joints in laminate robots is relatively standardized [54], however generation of linear actuation motions within laminate robotics has been less explored and typically requires exceptional design considerations such as custom actuators [55] or new transmission mechanisms [56, 57].

In this study we present the design and evaluation of a small-scale laminate robot that is actuated by a novel prismatic mechanism and capable of high-speed ground locomotion (relative to body size). We present this study in three sections. In the first section we describe the design and fabrication of the milliscale push–pull robot that uses two pairs of anisotropic bristles attached to a prismatic transmission. In the second section we describe the locomotion capabilities of this robot across a range of actuation parameters. In the last section of this study we present two models to describe the robot locomotion. We first present the deterministic push–pull model originally developed for quasi-static crawling behavior. We compare this model to our observations and conclude that it fails to capture the complexity of the robot speed-actuation performance. We next introduce a stochastic push–pull model, which captures the observed foot-slippage that occurs at higher frequencies and which is modeled as a stochastic phenomenon. Lastly, we describe the relationship between models and experiments and discuss opportunities for high-speed crawling based robotics.

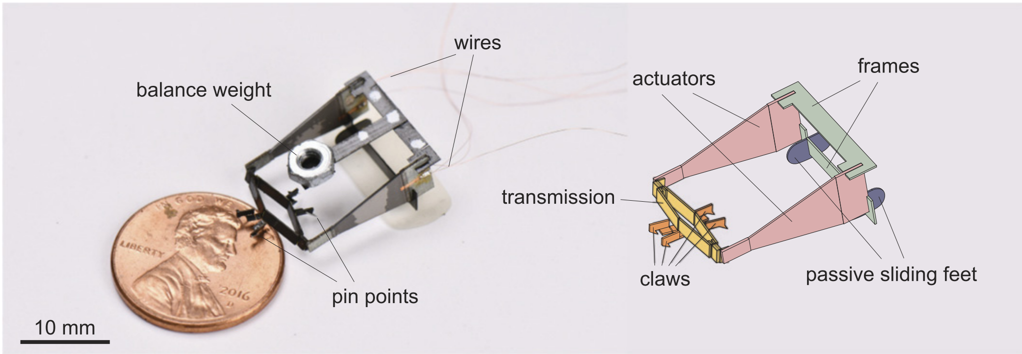

Figure 2. The 3P robot shown next to a United States penny for scale (left). The robot is composed of three main components: the transmission system, the actuators, and the robot frame (right).

2. Robot design

2.1. Overview

In this section we describe the design and fabrication of a milliscale robot that uses a prismatic transmission for push–pull locomotion. We call this robot 3P for simplicity due to the prismatic push–pull actuation. The 3P robot consists of a carbon-fiber chassis, two actuators, and a prismatic transmission, as shown in figure 2. The torso of the robot consists of two PZT actuators symmetrically assembled along the central longitudinal axis. The actuators connect to a prismatic transmission which transforms the lateral oscillations of the actuators into forward oscillations of the robot feet that approximate a linear motion along the fore-aft direction. Two pairs of flexible feet-like structures have bidirectional claws that engage with the ground substrate providing anisotropic friction. A balance weight and a skid plate allow the robot to remain stable on the ground with and without actuation. The robot weighs approximately 500 mg in total, which includes a 200 mg balance weight to adjust the center of mass. In the following sections we describe the robot design and fabrication in depth.

2.2. Actuation

The robot uses two bimorph PZT actuators to provide oscillatory inputs to the transmission. PZT actuators are chosen for three main reasons: (1) their fabrication process is relatively standardized and thus custom shapes can be created in the lab [52], (2) they provide high energy density (peak blocked force $\times$ peak free displacement) [58], and (3) can operate over a wide range of frequencies. Other means of actuating crawling robots such as shape memory alloy [15, 26, 44–46, 59], pneumatic actuators [16, 38, 41–43] and liquid crystal elastomers [19] suffer from time delays associated with heating and cooling and thus are not capable of high frequency actuation. Alternatively, other millimeter scale robots have used rotational vibratory motors for actuation [34, 35]. However, off the shelf vibratory motors are not able to independently change actuation amplitude, phase, and frequency.

Each PZT actuator is 15 mm in total length and the PZT plates have a trapezoidal shape with length, 10 mm, and bases of 1.5 mm and 6 mm on the narrow and wide ends, respectively. The actuators are custom fabricated using a diode-pumped solid-state (DPSS) laser, the details of the fabrication process have been thoroughly described elsewhere [52, 60]. The PZT plates are bonded to a central carbon fiber layer which acts to provide a conductive connection to the plates. The central carbon fiber layer also gives the actuator a relatively large bending stiffness and thus the PZT plates must generate force to overcome this intrinsic stiffness. While in many applications PZT actuators are matched to the system stiffness to achieve a resonance actuation phenomenon with a preferred frequency [4], in the design of 3P the actuators are oversized such that the output amplitude of the actuator and transmission system is constant over the frequency range of interest (see appendix A). Actuators of these size have a typical maximum output displacement of $\pm 250\ \mu$m.

The actuators are driven by a high-voltage PZT amplifier (PiezoDrive TD250) and each actuator requires a ground, bias, and signal voltage for actuation [61]. We connect the ground and bias signals together between the two actuators and thus the robot requires a total of four wires for actuation. The bias voltage is held at $V_B = 200$ V and the signal voltage is oscillated given by the function $V(t) = A\sin(2\pi ft) + \frac{V_B}{2}$ where the A is in the range of $A \in [0, \frac{V_B}{2}]$. Generation of the actuation signals are performed in Labview and a low-voltage analog output signals are provided to the amplifier to control the high-voltage signals through a National Instruments DAQ.

2.3. Transmission kinematics

Our robot is designed to perform an oscillatory crawling motion, to achieve this we designed a parallelogram based transmission inspired from [62], to provide a linear push and pull motion (figure 3(a)).

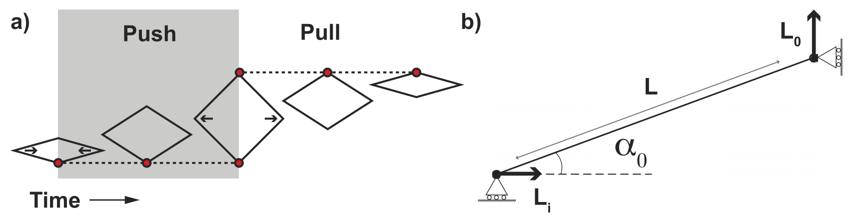

Figure 3. Push–pull locomotion and transmission kinematics. (a) Top-down view of the transmission movement. Over one oscillation cycle of the actuators the anisotropic feet engage the surface in a push and then a pull motion (red dots indicate foot engagement). (b) We consider the upper left quarter of the symmetric transmission to model the kinematics.

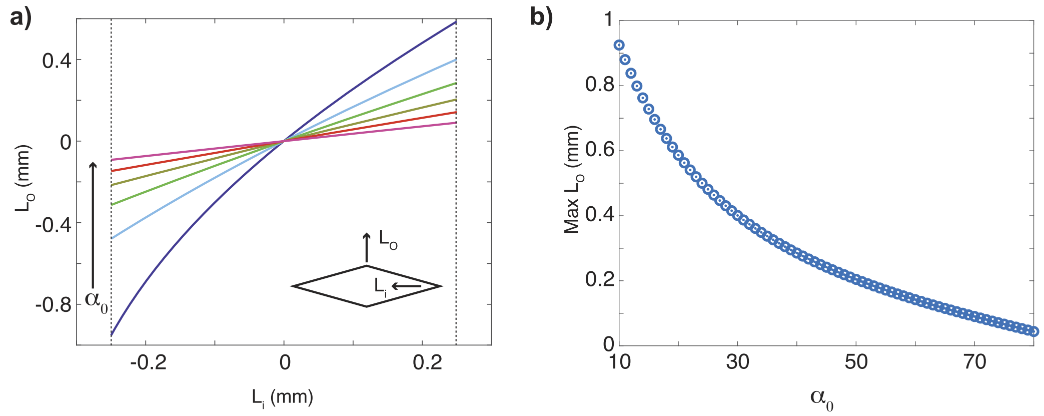

Figure 4. Transmission input and output displacement kinematics. The relationship between the input, L_i and output displacement, L_o, of the transmission for different initial angle configurations (left; $\alpha_0 = [10, 20, 30, 40, 50]$ with arrow showing direction of increase). The maximum output displacement for an input of $L_i = 250$ μm as a function of α_0 (right).

The design of mechanical transmissions for milliscale robots often requires the use of flexure hinges as opposed to true rotary joints [54]. Flexure-based compliant mechanisms are much easier to fabricate for milliscale systems, and they provide reliable motion that approximates true pin joints, although they can suffer from fatigue if appropriate materials are not chosen [63]. While numerous studies have been conducted to design, model, test, and analyze flexure based mechanisms [54, 64–66], in our treatment of the transmission kinematics we use a simplified symmetric four-bar linkage where we assume the flexure hinges are ideal pin joints (figure 3(b)).

We actuate the transmission with symmetric inputs from the left and right actuators. We assume that the actuators provide a horizontal input displacement to the left and right side of the transmission, and we assume the output displacement is in the fore-aft direction (figure 3(a)). Due to the symmetry of the transmission and input displacements we can simplify the modeling of the transmission kinematics by focusing on just one quarter of the parallelogram (figure 3(b)). An input displacement, L_i, in the horizontal direction generates an output displacement, L_o, in the vertical direction and drives the link, of length L, from an initial angle α_0 to α. The position relationship of the input and output points (in their horizontal and vertical directions, respectively) can be written as:

$$L\cos(\alpha_0) - L_i = L\cos(\alpha) \tag{1}$$

$$L\sin(\alpha_0) + L_o = L\sin(\alpha) \tag{2}$$

We can eliminate the variable α in equations (1) and (2) and solve for the output displacement L_o, retaining only the positive root

$$L_o = \sqrt{L^2\ \sin^2(\alpha_0) + 2LL_i\ \cos(\alpha_0) - L_i^2} - L\ \sin(\alpha_0) \tag{3}$$

To keep the width of our robot approximately 1 cm we chose a link length of $L = 5$ mm. The actuators we have chosen for our robot have a peak output displacement of ± 250 μm which places a constraint on the geometry of our transmission. For a fixed amplitude input, increasing the default parallelogram angle (α_0) results in a decrease of the transmission amplitude (figure 4). For low α_0 the transmission is moderately nonlinear while as α_0 increases the transmission becomes more linear.

We selected an α_0 of 10° for our transmission based in part on the kinematics and additional practical requirements of the robot. A low α_0 is favorable for our design because it provides a large amplification of displacement while requiring only modest bend angles of the flexure hinges. The flexure joints are approximated as pin joints for the purposes of

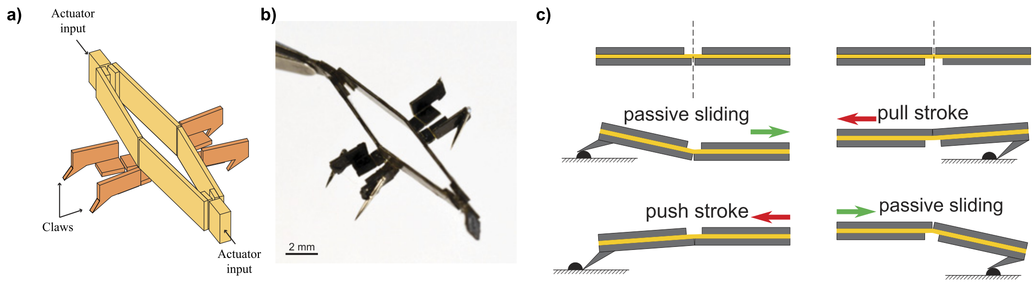

Figure 5. Transmission design and fabrication. (a) Isometric schematic of transmission showing actuator inputs on the left and right, and the pairs of push–pull claws. (b) Photo of completed linear transmission with claws. (c) Conceptual push–pull operation with passive flexures to enable sliding and locking of claws.

kinematic analysis, but in reality they provide a torsional resistance to bending roughly consistent with a torsional spring. Thus large flexure bend angles result in large internal torques that the actuators must overcome and may reduce the force output of the transmission. Lastly, a shallow transmission angle also enables easier fabrication because there is less internal elastic resistance in the transmission while it is being bent and assembled.

2.4. Transmission fabrication

The smart-composite manufacturing (SCM) method [67, 68] was used to build our robotic system. Our transmission was designed using a single laminate consisting of 25 layers as a single monolithic structure to reduce the number of folds which significant influence the assembly accuracy (figure 5). In appendix A we provide details of the laminate layers and geometry. Briefly, the SCM process involves multiple steps of laser cutting individual layers of structural (carbon fiber), flexure (Kapton), and adhesive (DuPont Pyralux) layers. These layers are bonded together in a thermal press and after multiple cut-and-cure steps the final transmission is laser cut from the surrounding multi-layer laminate.

Manual folding and gluing is required to complete the feet assembly and to attach the claws. The folding joints in figure 5(a) are folded 90° to form the foot structures shown in figure 5(b). The tips of four insect pins (#00, diameter = 0.27 mm) were removed and used as angled claws providing anisotropic ground friction. The claws were adhered to the transmission feet at approximately 45° with respect to horizontal plane [35]. Previous research has found that pins placed at an angle can increase the anisotropic friction coefficients between sliding and stance phase. Setting the pin angle to approximately 45° results in the claws engaging the highest amount of asperities as possible [18, 69]. To accommodate the uneven surface, we designed passive joints with an asymmetric joint stopper to allow the pin to accommodate different contact angles (figure 5(c)). This enhanced the engagement of the claws with ground during the thrust stroke while reducing friction during the passive return stroke.

3. Robot locomotion

We performed several experiments to identify the performance and behaviors of the sub-components of our robot (claws, transmission, actuators) in addition to studying the robot locomotion performance. First we measured the transmission kinematics and compared to theory. Next we measured the anisotropic friction performance of the bi-directional claws and body. Lastly we studied the forward motion of the robot under self-actuation in an unconstrained and a linearly constrained experimental configuration.

3.1. Transmission kinematics experiment and model comparison

To study the transmission kinematics under prescribed input displacement we assembled a benchtop testing station. The linear transmission and two bimorph piezoeletric (PZT) actuators were assembled together onto an acrylic testing base (figure 6(a)). A single high speed camera (Phantom VEO410) was used to capture the motion of the transmission and viewed the transmission perpendicular to the input and output motions. The actuators were calibrated such that the two actuator tips provided identical displacement inputs to the left and right side of the transmission, figure 6(b) (left). We tracked the motion of the transmission input and output using the DLTdv5 package in Matlab [70]. The input motion was prescribed to be sinusoidal, and the output motion of the transmission was observed to be an asymmetric periodic function (figure 6(b)).

We compared the experimental tip displacement to analytical results from the model using the same geometric dimensions from the design. The experimental output amplitude was smaller than that from the model prediction (equation (3)). It is likely that the output transmission kinematics are over predicted by the model because the rotational flexures are modeled as ideal pin joints, when in reality they can compress and bend with non-zero radius of curvature. Similar disparities between flexure and ideal joint modeling has been previously demonstrated [64]. To improve our model of the kinematics we adjusted the effective transmission length L using a

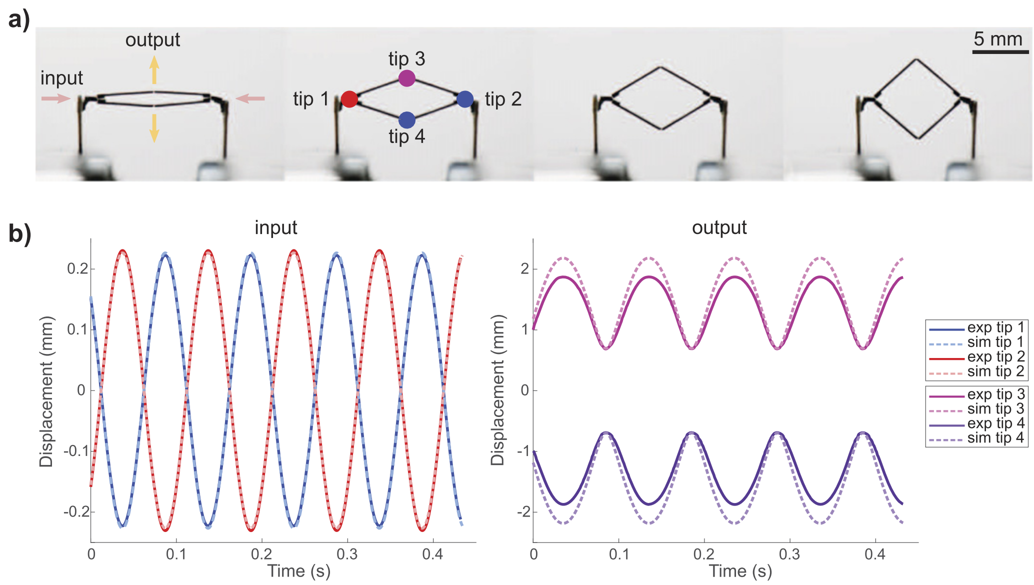

Figure 6. Transmission test results. (a) Linear transmission on testing stage. (b) Comparison of input and output motion of the linear transmission in experiments and simulation.

least-squares fitting routine. We found that an effective transmission length of $0.6L$ provided good agreement between experiment and the model. These experiments demonstrated that the transmission was capable of smooth and highly repeatable motion over a wide-range of input displacements and frequencies. Experiments up to frequencies of 250 Hz did not result in significant amplitude change (see appendix A for frequency sweep) indicating that dynamic effects of the transmission can be ignored in future analysis.

3.2. Anisotropic friction from angled claws and body

The robot claws slide across the substrate in the forward and backwards direction along the direction of movement (figure 5). When the claws are sliding away from the robot body (in the forward direction) the friction ideally should be low, and when the claw is sliding back toward the robot body (in the backwards direction) the friction should be high.

To determine the peak backwards sliding force that the angled claws can provide for thrust we assembled a friction testing experiment and we performed two separate measurements. In the first experiment the robot was attached to a force sensor by a thin wire (FUTEK LSB200-FSH02663; 500 mN max rating). The force sensor was mounted on a motor controlled displacement stage (Thorlabs MT S50) which displaced the force sensor and robot at a constant speed of 2.3 mm s^{-1} in a direction that engaged the angled claws against the substrate. The robot was placed on a substrate of card stock paper (the same used for locomotion experiments). The robot was not actuated and we measured the sliding force of the claws against the card stock substrate, which resulted in a claw propulsion force measurement of 21.1 ± 3.4 mN. In a second experiment we held the force sensor fixed and we allowed the robot to pull itself forward against the force sensor. In these measurements we observed a range of peak propulsion forces from the claws with an average propulsion of 47 ± 18 mN average peak force. The observed forces in the second set of experiments were larger likely because the actuation of the foot (at 80 Hz) enabled the claw to secure optimal footholds at a faster rate than when the robot was passively dragged. From these force measurements we estimate that the coefficient of friction for each claw in the propulsion direction is $\mu_+ = 9.6$. It is not unexpected for angled claw-like objects interacting with rough surfaces to have a friction coefficient substantially greater than unity [71].

To verify the force asymmetry from the claws we also determined the resisting force acting against the forward motion of the robot. To measure the stopping force against the robot we measured the dynamics of the robot coming to rest from a constant initial velocity, v. We used a high-speed camera to record the stopping of the robot while passively sliding and coming to rest. We computed the resistive force coefficient acting against the robot by fitting the position versus time with a constant resisting force μmg. We measured a resistive force friction coefficient of $\mu_- = 0.33$ corresponding to a resistive force of 1.62 mN acting against the forward motion of the robot. These experiments provided quantitative measurements of the force asymmetry from the angled claws and demonstrate that this robot has a force ratio of approximately 40 times in propulsive force compared to resistive force.

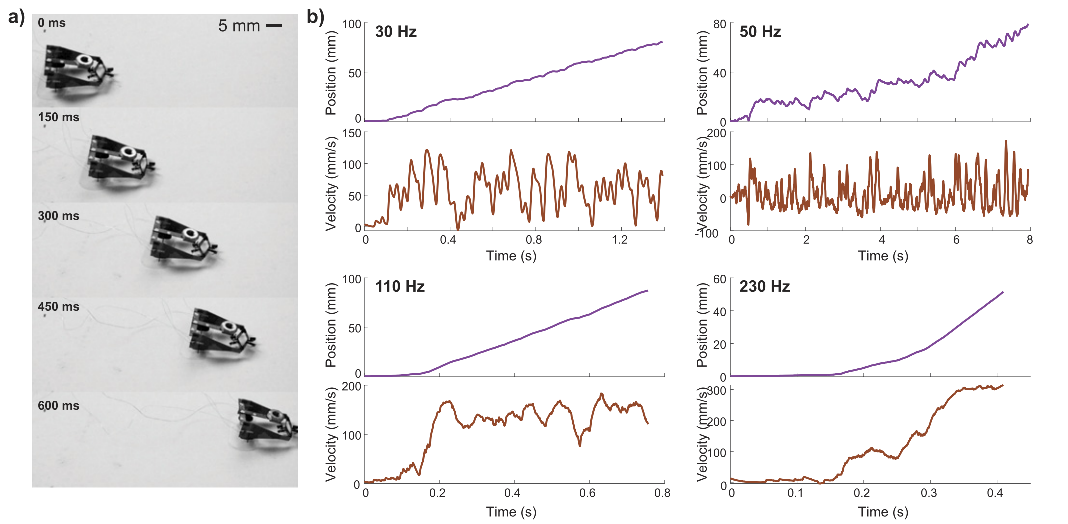

Figure 7. 3P robot locomotion examples. (a) Example of 3P robot moving from left to right at 90 Hz driving frequency. (b) Four examples of position and velocity versus time for the 3P robot moving at different driving frequencies.

3.3. Robot locomotion performance

We investigated the locomotion performance of the robot on card stock paper across a range of actuation frequencies. Two high-speed cameras with frame rate set to 20 times the driving frequency were used to capture the motion of the robot from side and top view, which enabled 3D reconstruction of the robot motion profiles. We conducted two sets of experiment: (1) the robot was confined move along a straight line by two bounding walls, and (2) the robot was able to move freely over the surface. We provide further details of the experimental setup in appendix A.

In figure 7 we show several examples of the position and velocity of the robot for four driving frequencies when the robot was unconfined. The robot position was tracked using the DLTdv5 package, and the velocity was estimated using Kalman filters based on the tracked position data. At low driving frequencies, for example 30 Hz, the velocity of the robot has large velocity fluctuations at the same frequency as the actuation (30 Hz). The robot body motion exhibits behavior that is reminiscent of a stop-start type of locomotion, which is also consistent with a previously described model of two-anchor locomotion in which the body is accelerated from rest at the beginning of the half-cycle and then comes to rest at the end of the half-cycle [1]. However, the stochastic nature of the body velocity indicates that the robot body does not come to rest exactly at the end of every half-cycle and suggests a possible importance of stochastic foot-ground interactions in the robot locomotion.

At higher driving frequency, for example 50 Hz, the velocity of the robot continued to display high-frequency fluctuations at the driving frequency. However, as actuation frequency increased we observed that the robot did not always come to rest at the end of the actuation cycle indicating that the robot had begun to slide forward near the end of a half-cycle. This suggests that at higher frequencies the locomotion behavior starts to violate the quasi-static assumption which requires that forward motion only occurs while the robot is actively pulling against the ground.

At frequencies above 110 Hz the instantaneous velocity of the robot was relatively smooth and greater than zero, indicating the presence of a substantial gliding type of motion propelled by the sequential acceleration and deceleration from the oscillatory claw movements. The relatively smooth velocity fluctuations at these high frequencies compared to lower frequency (approximately below 110 Hz) may be the result of foot slippage during the forward acceleration phase of the half-cycle. For the body to move in a no-slip manner the friction force must be larger than the required inertial acceleration, which for a purely sinusoidal foot motion would be $mA\omega^2$.

The overall kinematic relationship between actuation frequency and average speed is shown shown in figure 8. In both the free-run and the tunnel-run experiments we observed a similar trend in the speed–frequency relationship. We observed an approximately linear increase in average velocity with driving frequency from 10 Hz to 100 Hz. The average velocity reached a plateau from frequencies 100 Hz to 170 Hz, and then increased again at frequencies higher than 170 Hz. In the free-run and tunnel-run experiments we observed a sharp decrease in speed at 50 Hz, which we correlated with a body resonance mode in which large vertical vibration could be observed in the high-speed videos. In the tunnel-run experiments we performed testing at two actuator amplitudes (figure 8(a)) and we observe a speed decrease for the lower amplitude experiments with a similar trend in the non-linear speed–frequency relationship.

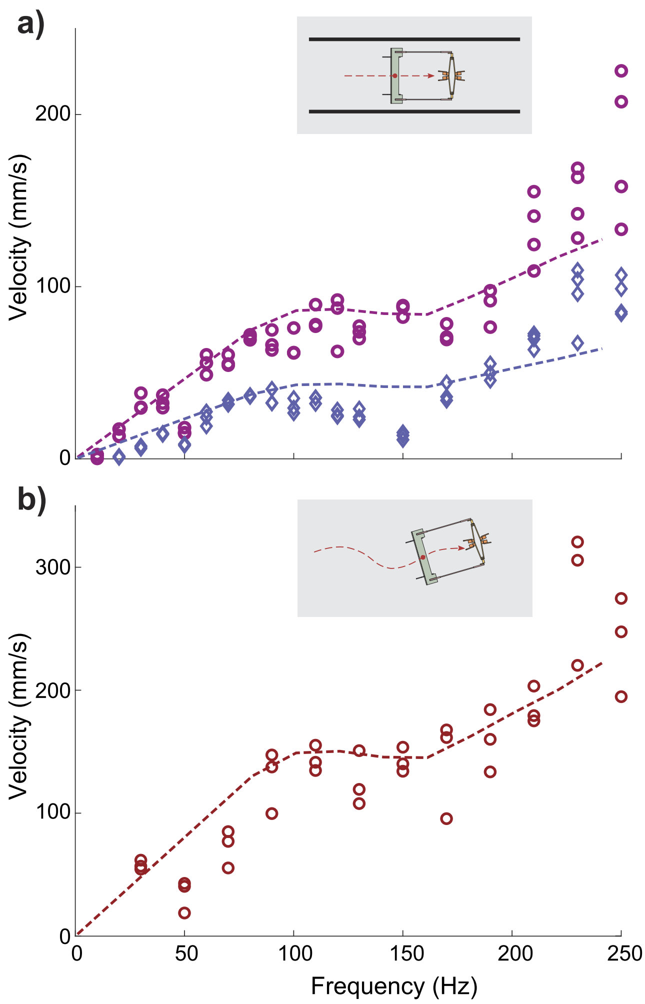

Figure 8. Average velocity of 3P robot across different driving frequencies. (a) 3P experiments performed in tunnel to enforce linear motion. Purple circles indicate experiments where the robot were driven at full amplitude. Blue diamonds indicate experiments where the robot were driven at half amplitude. Dashed lines are results from model developed in section 4. (b) 3P robot experiments without walls. Full amplitude experiments are shown in red circles.

The velocity trends are similar between the robot experiments in the constrained tunnel and on the unconstrained substrate. The primary difference between these experiments is that the average velocity of the robot was higher in the unconstrained substrate experiments compared to the tunnel experiments. In the tunnel experiments, the robot was constrained to move in a straight direction and thus collisions between the robot and the walls likely result in an average decrease in the robot speed. The vertical oscillation of the robot which is characterised by the standard deviation of vertical displacement increases linearly with driving frequency.

To determine the relative motion of the claws with respect to the ground we tracked the position of the robot claws across all frequencies in the free-run experiments. We specifically seek to determine the occurrence of claw slipping, which can occur in the forward direction (expected because of the low coefficient of forward friction) and potentially in the backward direction if the actuators exceed the friction force the claws can support during propulsion. In previous models of two-anchor crawling foot slipping was not considered and thus the average speed would be expected to increase linearly with increased oscillation frequency [1]. However, Coulomb friction is present in nearly all robots foot–ground interactions and thus understanding the prevalence claw slipping is important [72–74]. For our analysis we assume a claw can be in one of three possible states: (1) approximately stationary with respect to the ground when the magnitude of the claw velocity is below a velocity threshold of 35 mm s^{-1}, (2) slipping forwards away from the body with positive claw–ground velocity along the direction of motion either through forward body gliding, or during the second half of the actuation cycle in which the claw is being reset for the thrust phase, (3) slipping backwards toward the body with negative claw–ground velocity, which only occurs when the claw is slipping during the power stroke of the thrust.

Claw tracking reveals that there is a strong frequency dependence to the claw–ground interaction (figure 9). At low actuation frequency the claw

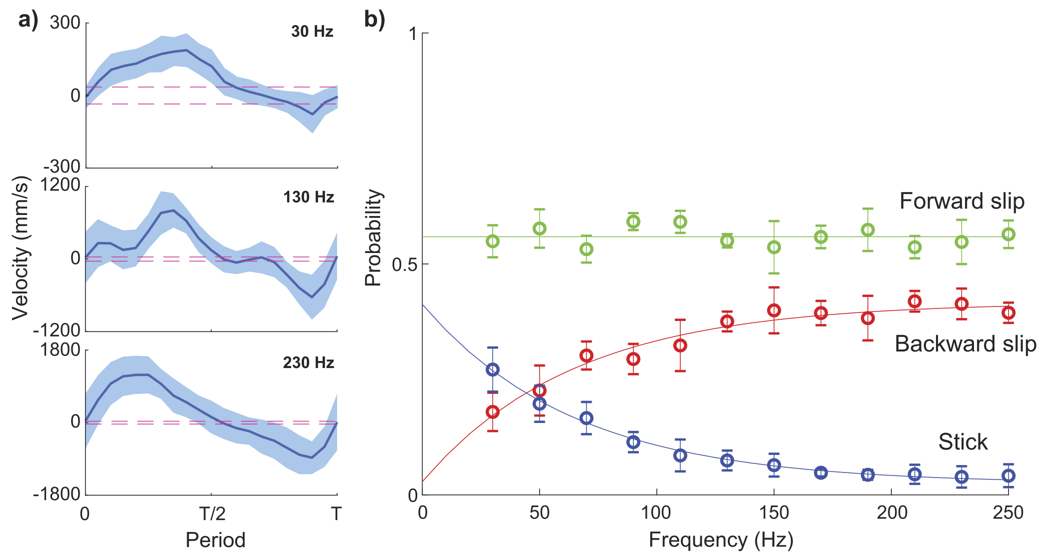

Figure 9. Robot foot tracking results. (a) Foot velocity in one period at low (30 Hz), intermediate (130 Hz), and high (230 Hz) frequencies. Red dash lines represent the threshold of whether the foot is assumed to be stationary with the ground (sticking) or not. (b) Ratio of foot status in one period across different frequencies.

slips during the propulsion phase of the actuation approximately 20% of the time (figure 9(b)) while the claw remains in approximate stationary contact approximately 30% of the time. As the actuation frequency is increased the probability to observe the claw slipping during the propulsion phase (backward slip) increased. The relative ratios of forward slip, backward slip, and approximately stationary are well fit by three functions that cumulatively are constrained to sum to probability 1 for each frequency. The forward slip probability is constant across frequency, given by $P_{\text{forward}} = 0.559$. However, the backward slip and approximate sticking probabilities are fit by saturating exponential curves, $P_{\text{stick}} = 0.388 \times \exp(-0.015 \times f){+}0.024$ and $P_{\text{backward}} = -0.388 \times \exp(-0.015 \times f) + 0.417$. The frequency dependence of the claw slipping behavior is likely correlated with the increased robot vibration that we observe as frequency increases. If the robot is excited by a high-frequency actuator it can cause body vibrations that can dislodge the engaged claw and likely result in the increased slipping probability we observe.

4. Dynamics of push–pull locomotion

The nonlinear speed versus frequency behavior of the robot motion is surprising given previous studies of two-anchor crawling locomotion [1]. The simplest approach to modeling two-anchor locomotion assumes that no-slipping occurs and thus the average robot speed should be a linear function of the actuation frequency. However, friction dynamics of vibration based locomotion are extremely important such as in anisotropic friction vibration based robots [34, 35] as well as stick-slip isotropic friction robots [37, 75]. To understand the relationship between speed and frequency for our robot we now will develop a mathematical model of two-anchor locomotion that considers both forward and backward slipping of the foot.

The organization of this section is as follows. We first introduce the notation for a deterministic two-anchor model in which the claw–ground interaction is determined solely by anisotropic Coulomb friction. We present the results of this model using parameters informed from our experiments and observe that this model lacks the ability to model the mid-frequency plateau we observe in speed. Next, we introduce a stochastic claw–ground slipping probability into our model to account for the frequency dependent claw–ground interaction. The inclusion of this increased probability to slip at increased frequency generates a speed–frequency that captures the nonlinear plateau we observe in our data. Previous models of two-anchor locomotion have been developed and extensively analyzed in previous works [21, 23], however our approach differs in two fundamental ways: (1) instead of controlling the actuation force between the two-anchors we impose time-dependent kinematics and solve for body movement, and (2) we incorporate probabilistic slip events inspired from our observations of frequent stochastic foot slipping.

We developed a simple model for the push–pull locomotion of our robot (figure 10(a)). In this model, we assume the robot with mass m is driven by sinusoidal push–pull motion of two claws and thus we neglect any potential dynamics that could be present in the actuation system. This decision is supported by the relatively small change in transmission amplitude versus frequency (see appendix A). We impose time-dependent kinematics of the position of the two claws

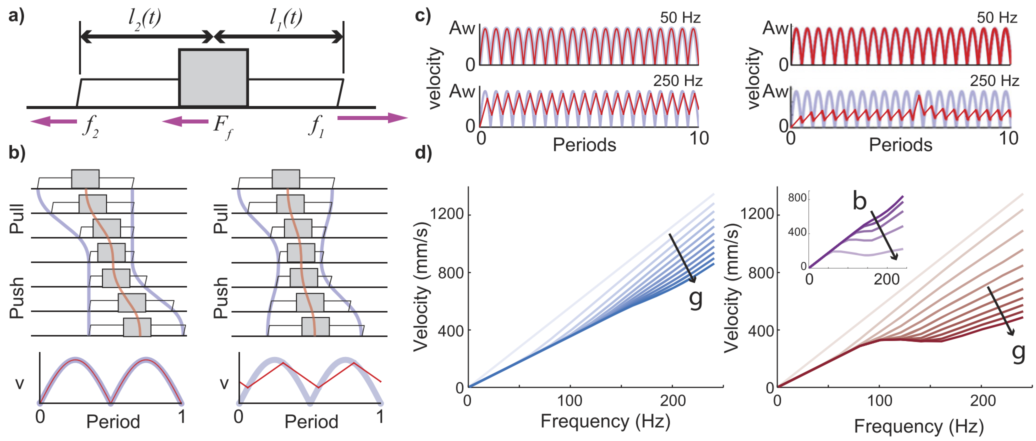

Figure 10. Model of push–pull locomotion dynamics. (a) Sketch of push–pull model. (b) Examples of low (left) and high (right) frequency dynamics in a deterministic model. Blue lines represent reference velocities of robot body with no-slip claw engagement. Red solid lines represent robot body velocities in the simulation. (c) Velocity examples of the deterministic (left) and the stochastic model (right) at low (50 Hz) and high (250 Hz) frequencies with $\gamma = 1.0$. Blue lines represent reference velocities of robot body with no-slip claw engagement. Red solid lines represent robot body velocities in the simulation. Time is scaled to period of oscillation, and velocity is scaled to $A\omega$. (d) Velocity prediction of the deterministic (left) and the stochastic (right) model with force ratio γ increasing as designated by arrow (from 0 to 1). In stochastic simulations $\beta = 0.3$. Inset on right plot illustrates variation as β is changed from 0.9 to 0.1 ($\gamma = 1.0$).

measured with respect to the body

$$l_1(t) = A \ \cos(\omega t) \tag{4}$$

$$l_2(t) = -A \ \cos(\omega t) \tag{5}$$

where A is the amplitude of claw oscillation and $\omega = 2\pi f$, where f is the actuation frequency.

As the two claws move with respect to the body they generate ground reaction forces f_1, f_2 (figure 5(a)). A positive ground reaction force indicates a thrust force propelling the robot in the forward direction, a negative ground reaction force is a braking force acting against forward motion. We assume that the claw forces interact only through anisotropic friction with a force range

$$F^- \leqslant f_i \leqslant F^+, \quad i = 1, 2 \tag{6}$$

where F^+ and F^- represent the maximum thrust force ($F^+ > 0$) and the maximum braking force ($F^- \leqslant 0$) of the claws.

During the pull stroke, the leading claw retracts toward the body and provides a positive force, while the trailing claw retracts toward the leading foot and slides passively on the ground generating a negative force $f_2 = F^-$. At the beginning of the push stroke the claws are near each other, the claws push away from each other and the trailing claw provides a positive force while the leading claw extends away from the body and slides passively on the ground generating resisting force $f_1 = F^-$. The push–pull motion is illustrated in figure 10(b). Throughout the push and pull motions the robot chassis passively slides on ground, generating a friction force:

$$F_f = \mathrm{sign}(\dot{x}_\mathrm{b})\mu mg \tag{7}$$

where $\dot{x}_\mathrm{b}$ is the velocity of the robot, μ is the coefficient of friction of the robot chassis, and g is gravity.

When a claw's velocity with respect to the ground is zero, then the foot is stationary and we call the foot anchored. The equation of motion of the robot when a propelling foot is anchored is given by the following:

$$m\ddot{x}_\mathrm{b} = f_i + F^- + F_f \tag{8}$$

where $\ddot{x}_\mathrm{b}$ is the acceleration of the robot and, $i = 1$ during the pull stroke and $i = 2$ during the push stroke. The propelling foot undergoes a backward slip if the velocity of the foot is negative, which leads to a foot–ground force of:

$$f_i = F^+, \quad i = 1 \text{ at pull stroke; } i = 2 \text{ at push stroke} \tag{9}$$

and thus an equation of motion of:

$$m\ddot{x}_\mathrm{b} = F^+ + F^- + F_f \tag{10}$$

Lastly, the propelling foot slips forward when the velocity of the foot is positive. In this case the foot–ground force is

$$f_i = F^-, \quad i = 1 \text{ at pull stroke; } i = 2 \text{ at push stroke} \tag{11}$$

thus

$$m\ddot{x}_\mathrm{b} = F^- + F^- + F_f \tag{12}$$

From the analysis above, we can simplify the ground-reaction forces from the multiple contact points to a maximum total thrust force and a maximum total resisting force that occur during the different phases of motion as:

$$F^+_\mathrm{max} = F^+ + F^- + F_f \tag{13}$$

$$F^-_\mathrm{max} = F^- + F^- + F_f \tag{14}$$

From this observation of a maximum and minimum force range of the robot we defined a ratio of the force asymmetry between F^{+}_{max} and F^{-}_{max} as:

$$\gamma = \frac{\|F^{-}_{max}\|}{\|F^{+}_{max}\|} \tag{15}$$

Large γ corresponds to a highly anisotropic friction force, while when $\gamma = 1$ the friction force from the claws are isotropic with no distinction between F^{+} and F^{-}.

At each push and pull stroke, the claws are trying to propel the motion of robot body in a no-slip manner such that the body acceleration would be exactly equal to the acceleration of the transmission

$$a = A(2\pi f)^2 \cos(\mathrm{mod}\ (2\pi ft, \pi)) \tag{16}$$

If the required force to propel the body, $f_{eff} = ma$, is lower than the possible maximum frictional force of the engaged claw, $F^{-}_{max} \leqslant f_{eff} \leqslant F^{+}_{max}$, then the motion of the robot is completely described by the motion of the transmission (figure 10(b), left column) and the foot does not slip. Otherwise the required force exceeds the force limits of claws and the robot body and claws will slip on the ground (figure 10(b), right column).

We simulated the dynamic model by setting $F^{+}_{max} = A(2\pi f)^2$ with specific $f = 150$ Hz to represent the maximum total propelling force. We set $A = 0.89$ mm according to the tracking data of the transmission output amplitude in the robot locomotion experiments. The relationship between the average velocity and the actuation frequency is shown in figure 10(c) left column. The robot velocity increased linearly when $\gamma = 0$ there is no resisting force against the robot, which meant that the steady state of robot velocity was fully determined by the maximum velocity of the robot transmission $v_{max} = A(2\pi f)$. When γ is nonzero, the robot velocity as a function of frequency diverged from the top-speed ($\gamma = 0$) curve and resulted in lower speeds at the same actuation frequency compared to the $\gamma = 0$ case. Critically, when $\gamma > 0$ the robot undergoes a combination of sticking and slipping as it moves, determined by the force relationship between the resisting (F^{-}_{max}) and the propulsive (F^{+}_{max}) forces. At low frequency actuation the force limit F^{-}_{max} and F^{+}_{max} are large enough such that the robot does not slip in the forward (glide) or backwards (back-slip) direction and the velocity follows an exact positive half sin wave. However γ is increased, the robot experiences higher resisting force and thus the robot to does not glide at higher frequencies which results in the lowered average speed curves versus frequency (figure 10(c)). When $\gamma = 0$ the robot builds up speed by gliding faster and faster until reaching the terminal velocity determined by the maximum transmission speed.

The predicted velocity trend lines of the deterministic model do exhibit a slight nonlinear trend as a function of frequency. However, the extent of the velocity plateau did not match the observed experiments over a wide exploration of simulation parameters. Furthermore, our investigation of the claw slipping dynamics revealed that the robot feet were constantly slipping in the backwards direction during the propulsion phase even at low frequencies (figure 9). We included the effect of frequency-dependent claw slipping into the deterministic model described above by stochastically modulating the peak force that a claw can provide against the ground. The probability fit curves associated with the fit functions in figure 9 were used to determine the peak claw force of a sticking event.

During the beginning of each propulsion stroke we randomly assigned the claw to either stick, or slip dependent on the frequency of actuation and the measured probability of sticking or slipping. If the claw was set to interact with with ground through sticking, we set $F^{+} = F_{high}$, while if the claw was set to slip backwards, we set $F^{-} = F_{low}$. This resulted in a range of maximum propelling forces based on the status of claws:

$$F^{+}_{max,high} = F_{high} + F^{-} + F_{f} \tag{17}$$

$$F^{+}_{max,low} = F_{low} + F^{-} + F_{f} \tag{18}$$

To parameterize the force difference between slipping and sticking forces during the propulsion phase we defined the ratio of $F^{+} = F_{high}$ and $F^{-} = F_{low}$ as:

$$\beta = \frac{F^{+}_{max,low}}{F^{+}_{max,high}} \tag{19}$$

Examination of the simulation behavior illustrates that inclusion of the frequency-dependent stochastic effect of claw slipping during the propulsion phase was able to reproduce the linear–plateau–linear speed–frequency relationship that we observed in experiment (figure 10). The magnitude of β determines the relative disparity between the propulsion force while sticking and while slipping. When $\beta = 1$ the slipping and sticking propulsion forces are the same, and when $\beta < 1$ then the slipping force is less than the sticking force (the most physically realistic case). We found that by inclusion of this stochastic slipping behavior the simple model captured the velocity behavior observed in experiment from low frequency to high frequency.

5. Discussion and outlook

We have presented the design of a millimeter-scale ground robot that operates using an inchworm inspired push–pull actuation strategy. This robot is able to operate at frequencies substantially higher than its biological counterparts or other previously developed worm-like robots. This robot shows substantially different speed–frequency results when compared to the theoretical predictions for deterministic push–pull locomotion. In particular the speeds we observed were well below what would be observed from a deterministic push–pull model suggesting potential complications to the modeling of claw–ground interaction. This discrepancy led us to the observation that the anisotropic claws exhibited substantial slipping, and that the fraction of time in which the claw was approximately stationary with respect to the ground diminished with increasing actuation frequency. By measuring the frequency dependent probability for the claw–ground states and including this into the model of push–pull locomotion we were able to capture the speed–frequency behavior of this robot.

Slipping is a common phenomena in legged locomotion. Sometimes slipping can be detrimental and result in falls or loss of thrust. However, slipping can also be beneficial as it allows a claw to potentially slip to a stronger foothold. In simplified models of legged locomotion we typically assume that the shear strength of a frictional foot-contact is determined by the normal force and coefficient of friction at that foothold. However, as our experiments highlight the shear resistance of frictional contacts can be variable and highly dependent on the claw and ground geometry [71]. In our experiments the friction variability is likely due to the heterogeneous structure of natural substrates such as the card-stock we use for our experiments. The strength of a frictional contact will encompass a range of possible values determined by the means of contact formation (how hard or gently the contact is formed for example), as well as the substrate heterogeneity.

Despite the significant foot slipping our robot exhibited it still was capable of relatively fast locomotion, with a maximum velocity of 434 mm s^{-1} (24 body lengths/s). The rapid speed is observed at the highest actuation frequency tested (250 Hz) and the speed–frequency trend is suggestive that higher speeds may be achievable at higher frequencies. Comparison of locomotion speed is complicated by the observation that smaller animals and robots tend to move faster on a relative scale (body lengths/s) but slower on an absolute scale. Compared to similar sized robots 3P is at the upper end of reported ground speeds for mobile robots that do not use wheels (see [76] for a comprehensive review of body size normalized robot speeds). Thus, through improvements in slip-resistance and actuation we may be able to achieve even higher speeds.

The high-frequency actuation of this robot enabled us to study a bio-inspired locomotion model well beyond the biologically relevant actuation regime. Actuating a robot with a worm-inspired locomotion strategy revealed that when foot slip is incorporated into a push–pull model we observe a nonlinear relationship between speed and frequency. This is an example of a broader class of experiments at the interface of biology and robotics which seek to use bio-inspired robots to study principles of movement. For example, recent experiments with a milliscale legged robot that is capable of actuation frequencies well outside the biological regime revealed a rich palette of locomotion modes not observed in animals [9]. Experiments that seek to elucidate general principles of locomotion will benefit from experimental platforms that encompass the range of natural locomotion but also enable us to look at the extremes to determine how well our models hold.

Acknowledgments

We thank members of the Gravish lab for helpful discussion and comments. Funding support was provided by the mechanical & aerospace engineering department at UC San Diego.

Appendix A

A.1. SCM method

The SCM method was developed to build robotic systems at the millimeter and centimeter scales, with features sizes down to tens of microns [67, 68]. SCM bridges the gap between traditional machining (meter to centimeter) and MEMS (micron to nanometer) fabrication. The SCM method uses multiple laminate layers that are all laser cut and laminated into a single composite sheet (figure 11). Layers are aligned and then cured in a heated platen press and then released to achieve desired micro structures by choice of design pattern and material properties (figure 11). SCM enables the integration of mechanical parts, such as links and joints, and electronic devices, such as PZT actuators, sensors, and wiring, into a complex microrobotic system [67].

Assembly accuracy is a significant challenge in microrobotics and specifically SCM based robots which require folding or manual bonding to achieve three-dimensional structure. Typical SCM laminates have five layers, two structural (carbon fiber), one flexural (Kapton), and two adhesive (DuPont Pyralux) (figure 12). Yet a robot component may be built from many of these five-layer laminates manually bonded together. In an effort to reduce the number of folds required to build our transmission we designed it using a single laminate consisting of 25 layers as a single monolithic structure (figure 5). Individual material layers are cut into 25 $\times$ 25 mm squares by a DPSS laser, containing complex in-plane features as small as 10 microns which is the resolution of the laser. Out-of-plane 3D mechanical structures are achieved by stacking carbon fiber structural layers, Kapton flexure layers, and adhesive layers along precision dowel pins which provide persistent lateral alignment. In the final transmission most material around the in-plane functional features are removed, however

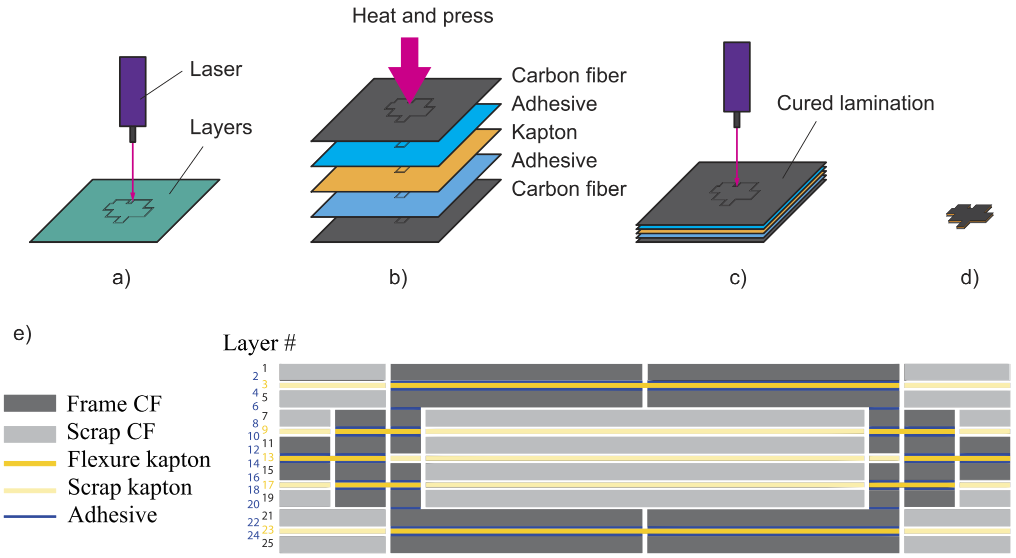

Figure 11. SCM method. (a) Laser cut individual layers. (b) A typical SCM laminate consists 5 layers in sequence (carbon fiber–adhesive–Kapton–adhesive–carbon fiber). Use heated platen press to form cured SCM laminate. (c) Laser cut to release the functional parts. (d) An example of released micro structure. (e) A detailed cross-section of the 25 layers used for the prismatic transmission.

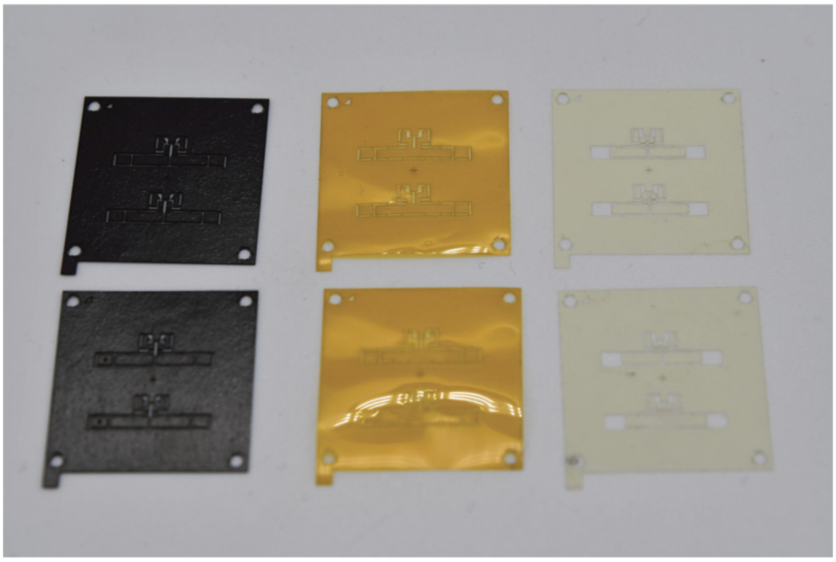

Figure 12. Selected examples of laser-cut individual layer. The black layers are structural carbon-fiber, the yellow layers are flexural Kapton, and the white layers are adhesive Pyralux.

for proper support during bonding we need to retain much of this scrap material for structural support. In the stacked multilayer laminate shown in figure 11(e), light gray parts of carbon fiber layers and light yellow parts of Kapton layers remain in-plane to provide out of plane support to the surrounding material during the press and cure process. After the transmission is laminated a final laser release cut is performed and the scrap material is removed leaving only the dark gray parts of the carbon fiber layers, dark yellow parts of the Kapton layers, and interleaved adhesive layers are retained. Carbon fiber forms the links of the linear transmission with $L = 5$ mm. The 0.1 mm Kapton gaps create revolute joints for the linear transmission.

A.2. Transmission dynamic response

To determine whether the dynamics of the transmission system influenced the locomotion speed–frequency behavior we sought to determine if the claws exhibited a resonance across the rang of tested frequencies. We tracked the output displacement of the transmission during the free-run experiments at all frequencies (figure 13). The result shows the amplitude of transmission does not change significantly across the frequencies we tested. Thus, we assumed the internal dynamic of the PZT actuator

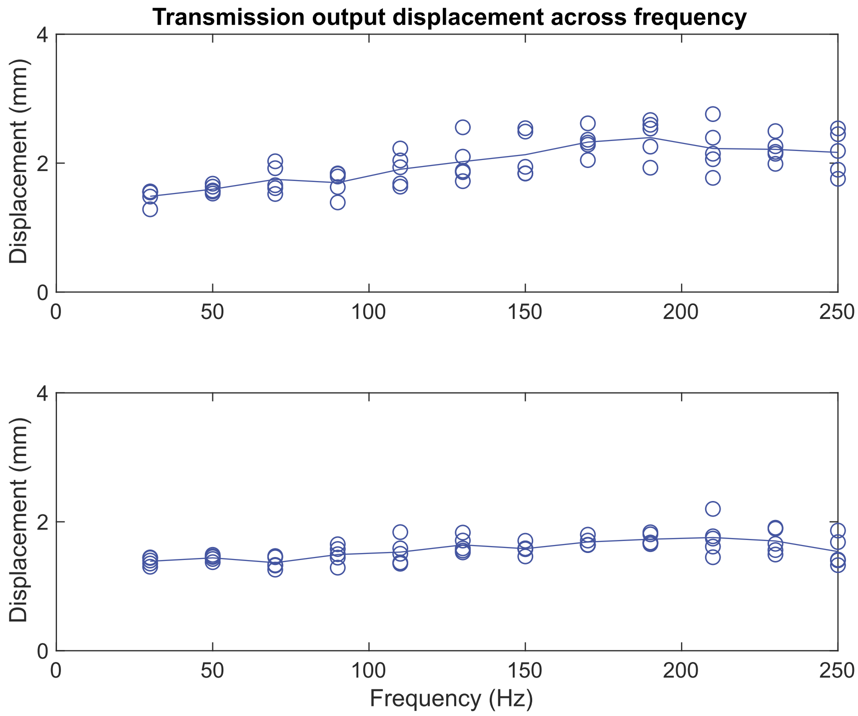

Figure 13. Dynamic response of transmission. Amplitude of transmission output of the upper claw (above) and lower claw (bottom) across different frequencies. The transmission performance remained consistent across frequency of interest.

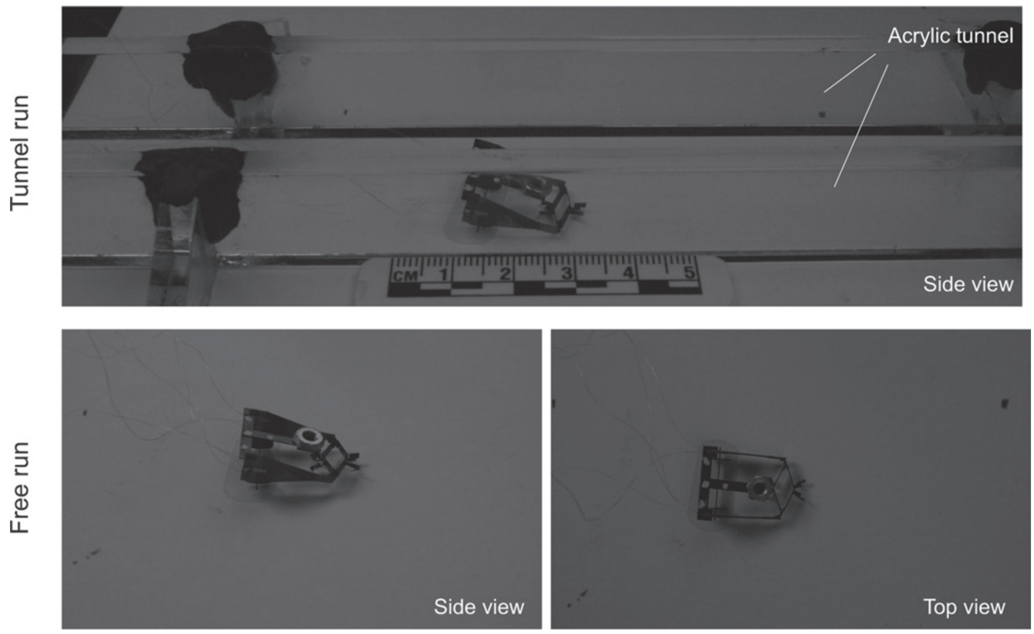

Figure 14. Robot experiment setup in tunnel run and free run.

and transmission system can be ignored when analyze the robot locomotion dynamic.

A.3. Locomotion testing details

We performed locomotion experiments using two experimental setups (figure 14). The first set of experiments were performed with the robot confined to move within a narrow channel. At the time of this work we had not integrated steering into robot and thus used the walls to enforce straight motion. The walls were made of transparent acrylic to enable high-speed camera viewing from the side. Figure 14 shows a view from the high-speed camera in the walled experiment. Free-run experiments were also performed and similar views are shown for the free run experiments. Two high-speed cameras were synchronized and used for all video data collection. Calibration enabled 3D reconstruction of the robot motion.

ORCID iDs

Wei Zhou https://orcid.org/0000-0001-7707-4022
Nick Gravish https://orcid.org/0000-0002-9391-2476

References

[1] Alexander R M N 2003 *Principles of Animal Locomotion* (Princeton, NJ: Princeton University Press)
[2] Dadashzadeh B, Vejdani H R and Hurst J 2014 From template to anchor: a novel control strategy for spring-mass running of bipedal robots *2014 IEEE/RSJ Int. Conf. on Intelligent Robots and Systems* pp 2566–71
[3] Renjewski D, Spröwitz A, Peekema A, Jones M and Hurst J 2015 Exciting engineered passive dynamics in a bipedal robot *IEEE Trans. Robot.* **31** 1244–51
[4] Ma K Y, Chirarattananon P, Fuller S B and Wood R J 2013 Controlled flight of a biologically inspired, insect-scale robot *Science* **340** 603–7
[5] Chang E, Matloff L Y, Stowers A K and Lentink D 2020 Soft biohybrid morphing wings with feathers underactuated by wrist and finger motion *Sci. Robot.* **5** eaay1246
[6] Di Luca M, Mintchev S, Su Y, Shaw E and Breuer K 2020 A bioinspired separated flow wing provides turbulence resilience and aerodynamic efficiency for miniature drones *Sci. Robot.* **5** eaay8533
[7] Marvi H *et al* 2014 Sidewinding with minimal slip: snake and robot ascent of sandy slopes *Science* **346** 224–9
[8] Astley H C *et al* 2015 Modulation of orthogonal body waves enables high maneuverability in sidewinding locomotion *Proc. Natl Acad. Sci. USA* **112** 6200–5
[9] Goldberg B, Doshi N, Jayaram K and Wood R J 2017 Gait studies for a quadrupedal microrobot reveal contrasting running templates in two frequency regimes *Bioinspiration Biomimetics* **12** 046005
[10] Brackenbury J 1999 Fast locomotion in caterpillars *J. Insect Physiol.* **45** 525–33
[11] Quillin K J 1999 Kinematic scaling of locomotion by hydrostatic animals: ontogeny of peristaltic crawling by the earthworm *Lumbricus terrestris J. Exp. Biol.* **202** 661–74
[12] Tettelbach S T, Europe J R, Tettelbach C R H, Havelin J, Rodgers B S, Furman B T and Velasquez M 2017 Hard clam walking: active horizontal locomotion of adult *Mercenaria mercenaria* at the sediment surface and behavioral suppression after extensive sampling *PLoS One* **12** e0173626
[13] Ellers O 1995 Form and motion of *Donax variabilis* in flow *Biol. Bull.* **189** 138–47
[14] Bruce C J 1986 Kinematics of terrestrial snake locomotion *Copeia* **1986** 915–27
[15] Kim B, Lee M G, Lee Y P, Kim Y I and Lee G H 2006 An earthworm-like micro robot using shape memory alloy actuator *Sensors Actuators* A **125** 429–37
[16] Lim J, Park H, An J, Hong Y-S, Kim B and Yi B-J 2008 One pneumatic line based inchworm-like micro robot for half-inch pipe inspection *Mechatronics* **18** 315–22
[17] Koh J-S and Cho K-J 2010 Omegabot: crawling robot inspired by *Ascotis selenaria 2010 IEEE Int. Conf. on Robotics and Automation* (IEEE) pp 109–14
[18] Lee D, Kim S, Park Y-L and Wood R J 2011 Design of centimeter-scale inchworm robots with bidirectional claws *2011 IEEE Int. Conf. on Robotics and Automation* (IEEE) pp 3197–204
[19] Rogóż M, Zeng H, Chen X, Wiersma D S and Wasylczyk P 2016 Light-driven soft robot mimics caterpillar locomotion in natural scale *Adv. Opt. Mater.* **4** 1689–94
[20] Zimmermann K, Zeidis I, Pivovarov M and Abaza K 2007 Forced nonlinear oscillator with nonsymmetric dry friction *Arch. Appl. Mech.* **77** 353–62
[21] Wagner G L and Lauga E 2013 Crawling scallop: friction-based locomotion with one degree of freedom *J. Theor. Biol.* **324** 42–51
[22] Bolotnik N, Pivovarov M, Zeidis I and Zimmermann K 2016 The motion of a two-body limbless locomotor along a straight line in a resistive medium *ZAMM-J. Appl. Math. Mech.* **96** 429–52
[23] Wu Z, Zhao D and Revzen S 2019 Coulomb friction crawling model yields linear force–velocity profile *J. Appl. Mech.* **86** 054501
[24] Umedachi T and Trimmer B A 2014 Design of a 3D-printed soft robot with posture and steering control *2014 IEEE Int. Conf. on Robotics and Automation (ICRA)* pp 2874–9
[25] Raymond H P 2015 Mathematical model of inchworm locomotion *Int. J. Non-Linear Mech.* **76** 56–63
[26] Koh J-S and Cho K-J 2013 Omega-shaped inchworm-inspired crawling robot with large-index-and-pitch (LIP) SMA spring actuators *IEEE/ASME Trans. Mechatronics* **18** 419–29
[27] Gidoni P, Noselli G and DeSimone A 2014 Crawling on directional surfaces *Int. J. Non-Linear Mech.* **61** 65–73
[28] Marvi H, Meyers G, Russell G and Hu D L 2012 Scalybot: a snake-inspired robot with active control of friction *ASME 2011 Dynamic Systems and Control Conf. and Bath/ASME Symp. on Fluid Power and Motion Control* (American Society of Mechanical Engineers Digital Collection) pp 443–50
[29] Ahmad R, Zhang Y, Liu B, Rubinstein S M and Bertoldi K 2018 Kirigami skins make a simple soft actuator crawl *Sci. Robot.* **3** eaar7555
[30] Tanaka Y, Ito K, Nakagaki T and Kobayashi R 2012 Mechanics of peristaltic locomotion and role of anchoring *J. R. Soc. Interface* **9** 222–33
[31] Liu B, Ozkan-Aydin Y, Goldman D I and Hammond F L 2019 Kirigami skin improves soft earthworm robot anchoring and locomotion under cohesive soil *2019 2nd IEEE Int. Conf. on Soft Robotics (RoboSoft)* pp 828–33
[32] Christensen D L, Suresh S A, Hahm K and Cutkosky M R 2016 Let's all pull together: principles for sharing large loads in microrobot teams *IEEE Robot. Autom. Lett.* **1** 1089–96
[33] Hu D L, Nirody J, Scott T and Shelley M J 2009 The mechanics of slithering locomotion *Proc. Natl Acad. Sci. USA* **106** 10081–5
[34] Majewski T, Szwedowicz D and Majewski M 2017 Locomotion of a mini bristle robot with inertial excitation *J. Mech. Robot.* **9** 061008
[35] Han Y, Marvi H and Sitti M 2015 Fiberbot: a miniature crawling robot using a directional fibrillar pad *2015 IEEE Int. Conf. on Robotics and Automation (ICRA)* pp 3122–7
[36] Shen Z, Liu Y, Zhao J, Tang X and Chen W 2017 Design and experiment of a small legged robot operated by the resonant vibrations of cantilever beams *IEEE Access* **5** 8451–8
[37] Du Z, Fang H, Zhan X and Xu J 2018 Experiments on vibration-driven stick-slip locomotion: a sliding bifurcation perspective *Mech. Syst. Signal Process.* **105** 261–75
[38] Ge J Z, Calderón A A, Chang L and Pérez-Arancibia N O 2019 An earthworm-inspired friction-controlled soft robot capable of bidirectional locomotion *Bioinspiration Biomimetics* **14** 036004
[39] Umedachi T, Vikas V and Trimmer B A 2016 Softworms: the design and control of non-pneumatic, 3D-printed, deformable robots *Bioinspiration Biomimetics* **11** 025001
[40] Umedachi T, Vikas V and Trimmer B A 2013 Highly deformable 3-D printed soft robot generating inching and crawling locomotions with variable friction legs *2013 IEEE/RSJ Int. Conf. on Intelligent Robots and Systems* pp 4590–5
[41] Shepherd R F, Filip I, Choi W, Morin S A, Stokes A A, Mazzeo A D, Chen X, Wang M and Whitesides G M 2011 Multigait soft robot *Proc. Natl Acad. Sci. USA* **108** 20400–3
[42] Gamus B, Salem L, Gat A D and Or Y 2020 Understanding inchworm crawling for soft-robotics *IEEE Robot. Autom. Lett.* **5** 1397–404

[43] Guo D and Kang Z 2020 Chamber layout design optimization of soft pneumatic robots *Smart Mater. Struct.* **29** 025017

[44] Huang X, Ford M, Patterson Z J, Zarepoor M, Pan C and Majidi C 2020 Shape memory materials for electrically-powered soft machines *J. Mater. Chem.* B **8** 4539–51

[45] Seok S, Onal C D, Wood R, Rus D and Kim S 2010 Peristaltic locomotion with antagonistic actuators in soft robotics *2010 IEEE Int. Conf. on Robotics and Automation* pp 228–1233

[46] Sugiyama Y and Hirai S 2006 Crawling and jumping by a deformable robot *Int. J. Robot. Res.* **25** 603–20

[47] Duduta M, Berlinger F, Nagpal R, Clarke D R, Wood R J and Temel F Z 2020 Tunable multi-modal locomotion in soft dielectric elastomer robots *IEEE Robot. Autom. Lett.* **5** 3868–75

[48] Pfeil S, Henke M, Katzer K, Zimmermann M and Gerlach G 2020 A worm-like biomimetic crawling robot based on cylindrical dielectric elastomer actuators *Frontiers Robot. Ai* **7** 1–9

[49] Zhang J, Wang T, Wang J, Li B, Hong J, Zhang J X J and Wang M Y 2019 Dynamic modeling and simulation of inchworm movement towards bio-inspired soft robot design *Bioinspiration Biomimetics* **14** 066012

[50] Rus D and Tolley M T 2015 Design, fabrication and control of soft robots *Nature* **521** 467

[51] Whitney J P, Sreetharan P S, Ma K Y and Wood R J 2011 Pop-up book MEMS *J. Micromech. Microeng.* **21** 115021

[52] Jafferis N T, Smith M J and Wood R J 2015 Design and manufacturing rules for maximizing the performance of polycrystalline piezoelectric bending actuators *Smart Mater. Struct.* **24** 065023

[53] Baisch A T, Ozcan O, Goldberg B, Ithier D and Wood R J 2014 High speed locomotion for a quadrupedal microrobot *Int. J. Robot. Res.* **33** 1063–82

[54] Doshi N, Goldberg B, Sahai R, Jafferis N, Aukes D, Wood R J and Paulson J A 2015 Model driven design for flexure-based microrobots *2015 IEEE/RSJ Int. Conf. on Intelligent Robots and Systems (IROS)* pp 4119–26

[55] Goldberg B, Karpelson M, Ozcan O and Wood R J 2014 Planar fabrication of a mesoscale voice coil actuator *2014 IEEE Int. Conf. on Robotics and Automation (ICRA)* pp 6319–25

[56] York P A and Wood R J 2017 A geometrically-amplified in-plane piezoelectric actuator for mesoscale robotic systems *2017 IEEE Int. Conf. on Robotics and Automation (ICRA)* pp 1263–8

[57] York P A and Wood R J 2017 A geometrically-amplified in-plane piezoelectric actuator for mesoscale robotic systems *2017 IEEE Int. Conf. on Robotics and Automation (ICRA)* (IEEE) pp 1263–8

[58] Wood R J, Steltz E and Fearing R S 2005 Optimal energy density piezoelectric bending actuators *Sensors Actuators* A **119** 476–88

[59] Noselli G and DeSimone A 2014 A robotic crawler exploiting directional frictional interactions: experiments, numerics and derivation of a reduced model *Proc. R. Soc.* A **470** 20140333

[60] Jafferis N T, Lok M, Winey N, Wei G-Y and Wood R J 2016 Multilayer laminated piezoelectric bending actuators: design and manufacturing for optimum power density and efficiency *Smart Mater. Struct.* **25** 055033

[61] Karpelson M, Wei G-Y and Wood R J 2012 Driving high voltage piezoelectric actuators in microrobotic applications *Sensors Actuators* A **176** 78–89

[62] York P A, Jafferis N T and Wood R J 2017 Meso scale flextensional piezoelectric actuators *Smart Mater. Struct.* **27** 015008

[63] Malka R, Desbiens A L, Chen Y *et al* 2014 *Principles of Microscale Flexure Hinge Design for Enhanced Endurance* IEEE/RSJ

[64] Lobontiu N and Garcia E 2003 Analytical model of displacement amplification and stiffness optimization for a class of flexure-based compliant mechanisms *Comput. Struct.* **81** 2797–810

[65] Ma H-W, Yao S-M, Wang L-Q and Zhong Z 2006 Analysis of the displacement amplification ratio of bridge-type flexure hinge *Sensors Actuators* A **132** 730–6

[66] Xu Q and Li Y 2011 Analytical modeling, optimization and testing of a compound bridge-type compliant displacement amplifier *Mech. Mach. Theory* **46** 183–200

[67] Wood R J, Avadhanula S, Sahai R, Steltz E and Ronald S F 2008 Microrobot design using fiber reinforced composites *J. Mech. Des.* **130** 052304

[68] Sreetharan P S, Whitney J P, Strauss M D and Wood R J 2012 Monolithic fabrication of millimeter-scale machines *J. Micromech. Microeng.* **22** 055027

[69] Asbeck A T, Kim S, Cutkosky M R, Provancher W R and Lanzetta M 2006 Scaling hard vertical surfaces with compliant microspine arrays *Int. J. Robot. Res.* **25** 1165–79

[70] Hedrick T L 2008 Software techniques for two-and three-dimensional kinematic measurements of biological and biomimetic systems *Bioinspiration Biomimetics* **3** 034001

[71] Dai Z, Gorb S N and Schwarz U 2002 Roughness-dependent friction force of the tarsal claw system in the beetle *Pachnoda marginata* (coleoptera, scarabaeidae) *J. Exp. Biol.* **205** 2479–88

[72] Woodward M A and Metin S 2018 Morphological intelligence counters foot slipping in the desert locust and dynamic robots *Proc. Natl Acad. Sci. USA* **115** E8358–67

[73] Zhao D and Revzen S 2020 Multi-legged steering and slipping with low DoF hexapod robots *Bioinspiration Biomimetics*

[74] Carius J, Ranftl R, Koltun V and Hutter M 2019 Trajectory optimization for legged robots with slipping motions *IEEE Robot. Autom. Lett.* **4** 3013–20

[75] Fang H and Xu J 2014 Stick-slip effect in a vibration-driven system with dry friction: sliding bifurcations and optimization *J. Appl. Mech.* **81** 051001

[76] Wu Y *et al* 2019 Insect-scale fast moving and ultrarobust soft robot *Sci. Robot.* **4** eaax1594